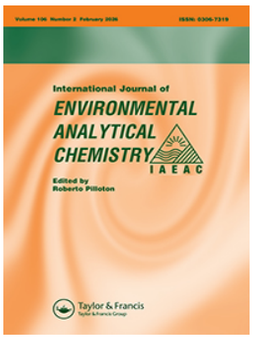

International Journal of Environmental Analytical Chemistry

ISSN: 0306-7319 (Print) 1029-0397 (Online) Journal homepage: www.tandfonline.com/journals/geac20

Sustainable sunlight-driven remediation of PAH-contaminated soil using a green, waste-derived nanocomposite

Shileer Sulaiman Omer & Soleyman Moinfar

To cite this article: Shileer Sulaiman Omer & Soleyman Moinfar (21 Jan 2026): Sustainable sunlight-driven remediation of PAH-contaminated soil using a green, waste-derived nanocomposite, International Journal of Environmental Analytical Chemistry, DOI: 10.1080/03067319.2026.2614317

To link to this article: https://doi.org/10.1080/03067319.2026.2614317

INTERNATIONAL JOURNAL OF ENVIRONMENTAL ANALYTICAL CHEMISTRY
https://doi.org/10.1080/03067319.2026.2614317

Sustainable sunlight-driven remediation of PAH-contaminated soil using a green, waste-derived nanocomposite

Shileer Sulaiman Omer[a] and Soleyman Moinfar[b,c]

[a]Environmental Science Department, University of Zakho, Zakho, Iraq; [b]Chemical Analysis Research Center, Scientific Research Center, University of Zakho, Zakho, Iraq; [c]Department of Basic Sciences, College of Pharmacy, Nawroz University, Duhok, Iraq

ABSTRACT

Polycyclic aromatic hydrocarbons (PAHs) are persistent soil pollutants posing serious environmental and health risks due to their toxicity, carcinogenicity, and resistance to degradation. A key challenge in remediating PAH-contaminated soils is achieving efficient, low-cost, and pollution-free degradation under natural sunlight. This study reports a sustainable Fe_3O_4/carbon dots/silver iodide (Fe_3O_4/CD/AgI) nanocomposite, synthesised entirely from waste-derived precursors including industrial iron waste and wheat straw, for the sunlight-driven photocatalytic degradation of PAHs in contaminated soil. Characterisation by FTIR, XRD, SEM, and TGA confirmed the successful formation and favourable structure of the composite. Under optimal conditions (0.2 g catalyst per 4 g soil, 48 h solar exposure), complete degradation of naphthalene and while anthracene and pyrene showed removal efficiencies of approximately 65% and 71%, respectively. The composite exhibited enhanced efficiency, especially when combined with sodium persulphate, due to the synergistic contributions of magnetic recovery by Fe_3O_4, broad light capture by carbon dots, visible-light responsiveness of AgI, and persulphate-activated generation of reactive oxygen species (•OH, $SO_4^{\bullet-}$, $O_2^{\bullet-}$). This study demonstrates that a fully waste-derived, sunlight-responsive nanocomposite can effectively degrade both low- and high-molecular-weight PAHs, offering a low-cost, environmentally friendly, and scalable strategy for in-situ soil remediation.

ARTICLE HISTORY
Received 12 November 2025
Accepted 5 January 2026

KEYWORDS
Polycyclic aromatic hydrocarbons; green Fe_3O_4 /carbon dots/AgI; photo-degradation; soil remediation; waste valorisation; GC-MS

1. Introduction

Soil contamination by polycyclic aromatic hydrocarbons (PAHs) has emerged as a major environmental concern due to their persistence, toxicity, and widespread occurrence in ecosystems [1]. PAHs are a class of organic compounds composed of two or more fused aromatic rings, primarily generated through the incomplete combustion of organic materials such as fossil fuels, biomass, and waste [2]. Although natural events like forest fires and volcanic eruptions can release PAHs, anthropogenic activities, including industrial emissions, vehicular exhaust, coal tar production, and agricultural burning are the

CONTACT Soleyman Moinfar soleiman_moinfar@yahoo.com; soleiman.moeinfar@uoz.edu.krd

dominant sources of PAHs pollution [3]. The chemical stability and hydrophobic nature of PAHs make them highly resistant to natural degradation, resulting in their accumulation in air, water, and soil [4]. This persistence poses serious long-term risks to the environment and human health, making PAHs a critical target for environmental remediation and public safety efforts [5,6]. In soil environments, PAHs represent a major hazard due to their strong sorption to soil organic matter, leading to long-term persistence and accumulation while disrupting microbial communities, nutrient cycling, and plant growth [7]. Contaminated soils can also release PAHs into groundwater or transport them via surface runoff, spreading contamination to aquatic systems. PAHs are toxic to aquatic organisms, including invertebrates, fish, and algae, causing DNA damage, reproductive disorders, and developmental abnormalities, thereby disturbing food webs and reducing biodiversity. Moreover, atmospheric deposition contributes to the long-range transport of PAHs, leading to the contamination of remote environments [8].

Health concerns related to PAHs are substantial, with compounds such as benzo[a] pyrene classified as carcinogenic by the International Agency for Research on Cancer (IARC) [9]. Prolonged exposure through inhalation, ingestion, or dermal contact has been linked to lung, skin, and bladder cancers, particularly among workers in coal tar refining and asphalt production industries. Prenatal exposure can cross the placental barrier, leading to low birth weight, developmental delays, and congenital abnormalities [10]. Emerging studies also suggest that PAHs may contribute to neurodevelopmental disorders and immune system suppression, emphasising the urgent need for effective mitigation strategies [11]. Research has shown that over 90% of PAHs in the natural environment are retained in soils, especially in areas near industrial facilities such as coking plants. This accumulation makes soil one of the most affected environmental compartments and a primary target for remediation efforts [12].

Over the past decade, numerous studies have explored strategies for remediating PAH-contaminated soils. However, most established methods still face significant limitations. Conventional remediation techniques – such as soil washing, thermal treatment, and bioremediation – have generally shown limited effectiveness [13]. In soil washing, solvents or surfactants are employed to extract PAHs from soil; however, the process is often costly, generates secondary waste, and is impractical for large-scale applications [14]. Thermal treatment involves heating the soil to volatilise or decompose PAHs, but it is highly energy-intensive and can lead to the loss of soil organic matter and beneficial microorganisms [15]. Bioremediation, which relies on microorganisms to degrade PAHs, is a more environmentally friendly approach; nevertheless, it is often slow and inefficient due to the low bioavailability and chemical stability of PAHs [13]. These limitations underscore the urgent need for innovative and sustainable remediation technologies capable of effectively degrading PAHs while minimising environmental impact and economic cost [16].

In recent years, nanomaterials have emerged as a promising alternative for environmental remediation [17], offering advantages such as high surface area, enhanced reactivity, and the ability to target specific pollutants [18]. Various nanomaterials have been investigated for PAH remediation, including titanium dioxide (TiO_2), zinc oxide (ZnO), graphene oxide (GO), and zero-valent iron (ZVI) [19]. While TiO_2 and ZnO are widely used photocatalysts, their activity is largely limited to ultraviolet (UV) light, which accounts for only a small fraction of solar radiation, thereby restricting their effectiveness under natural

sunlight [20,21]. Graphene-based materials provide high surface area and excellent conductivity; however, they lack intrinsic catalytic activity unless combined with metal nanoparticles [22]. Similarly, ZVI can facilitate Fenton-like reactions, but its application is constrained by poor long-term stability and particle aggregation in soil environments [23].

In this study, a Fe_3O_4/carbon dot/AgI (Fe_3O_4/CD/AgI) nanocomposite was synthesised for the first time, offering an environmentally friendly, sunlight-responsive alternative that overcomes many limitations of conventional nanomaterials. Fe_3O_4 nanoparticles provide magnetic properties that enable facile recovery and contribute to reactive oxygen species generation via Fenton-like mechanisms [24]. Carbon dots (CDs) derived from wheat straw enhance visible-light absorption and promote charge separation due to their high electron mobility [25]. Meanwhile, silver iodide (AgI), a visible-light-responsive semiconductor, further improves the photocatalytic performance of the composite through efficient photon absorption and effective charge separation [26]. Compared with silver nanoparticles, AgI demonstrates superior photocatalytic activity under solar irradiation owing to its narrower bandgap and enhanced production of reactive species [27]. The synergistic combination of Fe_3O_4, CDs, and AgI results in a multifunctional nanocomposite with broad-spectrum light responsiveness, magnetic recoverability, and highly efficient degradation of pollutants under natural sunlight [28].

This study presents an innovative green Fe_3O_4/CD/AgI nanocomposite, synthesised entirely from waste-derived precursors, for the efficient photodegradation of PAHs in contaminated soils under natural sunlight. Fe_3O_4 nanoparticles were prepared from industrial iron waste, and carbon dots were derived from wheat straw, exemplifying a sustainable, circular-economy-based approach. Incorporation of AgI significantly enhances light absorption and electron transport, enabling effective solar-driven photocatalysis. The ternary nanocomposite demonstrates high performance under ambient solar irradiation, offering a scalable, cost-effective, and environmentally sustainable strategy for in-situ soil remediation. This work represents the first application of Fe_3O_4 derived from iron waste combined with biomass-derived carbon dots and AgI for visible-light-driven restoration of PAH-contaminated soils, providing a practical, eco-friendly, and efficient approach to mitigating persistent organic pollutants in terrestrial ecosystems. Additionally, the use of industrial and agricultural waste as raw materials reduces the need for virgin mineral resources and minimises associated carbon emissions, offering clear environmental benefits. From a life cycle perspective, such green synthesis strategies can significantly decrease the ecological footprint of catalyst production, aligning this work with current sustainable development goals [29,30].

2. Materials and methodology

2.1. Chemicals and materials

All materials and solvents were of analytical grades and used without purification. Acenaphthylene, fluorene, phenanthrene and pyrene were purchased from BLD PHARMATECH (GmbH, Germany). Fluoranthene were purchased from thermo scientific (China). Naphthalene was obtained from Sigma-Aldrich (Germany), anthracene was purchased from OEA Labs Ltd., (UK). In addition, dichloromethane, methanol were

purchased from Carlo Erba Reagent (Italy). Acetone was obtained from Carlo Roth GmbH Co. (KG, Germany). AgNO3 was purchased from thermo scientific (Germany). KI, NaOH were purchased from Sicco Research Laboratories Pvt. Ltd. (India). HCl was purchased from sigma Aldrich (USA). Na2S2O8 was obtained from Alfa Aeser (Germany). Urea was obtained from Merck Life Science (Germany). Industrial iron waste was obtained as a waste by-product from a local blacksmith's workshop. Wheat straw, an agricultural residue, was collected from farmlands in the Zakho region (northern Iraq). Polyvinylpyrrolidone (PVP) was purchased from carlRoth (Germany). In this study, seven representative PAHs – naphthalene, acenaphthylene, fluorene, phenanthrene, anthracene, fluoranthene, and pyrene – were selected primarily because these include both low- and high-molecular-weight PAHs with varying molecular structures, hydrophobicity, persistence, and resistance to degradation, allowing a comprehensive evaluation of the photocatalytic performance of the Fe_3O_4/CD/AgI system.

2.2. Instruments

An ultrasonic cleaner (Elmasonic P180H, Elma, Germany) was used for ultrasonic-assisted extraction. A rotary evaporator (BUCHI, Switzerland) was employed to removing excess solvent under reduced pressure. The nanocomposite was synthesised and dried in a Thermo Scientific Heratherm Oven (Germany). The pH values were measured with a mettler Toledo AG pH metre (Switzerland) supplied with a glass combined electrode. The hotplate stirrer (Korea) was used to provide controlled stirring. Samples were centrifuged using a Hettich Universal 320 centrifuge (Germany).

The scanning electron microscopy (SEM) was conducted at 15.0 kV on an electron microscope (LEO 1430VP, Germany). The X-ray diffraction (XRD) patterns were obtained on a diffractometer (X-Pro, Philips, Netherland) using Cu-Kα radiation (λ = 1.5418 Å) in the angular region (2θ) of 5–80°. The FTIR spectra were obtained using an FTIR spectrometer (Spectrum RXI, PerkinElmer, USA). A thermal analyser (STA PT-1000, Linseis, Germany) was used to conduct thermal gravimetric analysis (TGA).

2.3. GC-MS conditions

A Clarus 580 gas chromatography systems (PerkinElmer, USA) equipment with Rst-5 MS capillary column (30 m, 0.25 µm film thickness, and 0.25 mm inner diameter) from Resteck (USA) was used to analyse extracted PAHs. The GC system was coupled with a Clarus SQ 8S mass spectrometer (PerkinElmer, USA), featuring a quadrupole analyser to perform GC-MS analyses. The analysis was conducted using the helium gas 99.999% (Air Products, UK) as carrier gas, at a flow rate of 1 mL/min. The temperature settings for the ion source and mass spectrometry transfer line were set at 220°C and 235°C, respectively. By means of this procedure, in split injection mode, a 20:1 split ratio was employed. The conditions for the analytical procedure for GC-MS were: an inlet temperature of 290°C; the initial temperature for the GC oven was set from 100°C to 190°C, for doing this the temperature ramping was carried out at 15°C/min with a holding time of 1 min. Afterwards, heating up to 270°C at a rate of 12°C/min was done, and retained for 2 min.

2.4. Synthesis of photocatalysts

2.4.1. Synthesis of carbon dot from wheat straw

Carbon dots (CDs) were manufactured via a one-step hydrothermal processes derived from a biomass-based technique [25]. In summary, 2.0 g of desiccated wheat straw powder was suspended into 50 mL of deionised water then stirred for 2 hours. The mixture was thereafter placed in a Teflon-lined stainless steel autoclave and subjected to heating at 185°C for 6 hours. Following natural cooling to ambient temperature, the resultant suspension was centrifuged at 1000 rpm for 10 minutes to eliminate bulk residues. The supernatant was filtered using a 0.22 µm membrane resulting in pure CDs, which were subsequently kept in dark glass vials for future application.

2.4.2. Synthesis of Fe_3O_4 nanoparticles

A precursor iron solution was prepared from waste iron using a modified acid leaching method [31]. In brief, 5.0 g of iron waste was thoroughly washed with deionised water to remove surface contaminants, dried at room temperature, and separated magnetically. The dried material was then dissolved in a mixture of 15 mL concentrated hydrochloric acid and 5 mL deionised water in a sealed glass container and left undisturbed at room temperature for 24 hours. The solution was filtered to remove undissolved solids, and the resulting clear iron solution was collected and stored in a sealed container for later use. To synthesise iron oxide nanoparticles, 5 mL of this iron solution was mixed with 5.0 g of urea and subjected to 30 minutes of ultrasonication. Sodium hydroxide (0.25 M) was gradually added under continuous stirring until precipitation occurred or the pH reached 12. The precipitate was washed with deionised water, dried at 60–80°C for 24 hours, and stored in an airtight container, yielding well-controlled, high-quality iron oxide nanoparticles.

2.4.3. Synthesis of green Fe_3O_4/CD nanocomposite

A green nanocomposite of iron oxide and carbon dots was created by combining 5 mL of iron (Fe) solution, 5 mL of carbon dots solution, and 5.0 g of urea in a reaction vessel. The mixture was subjected to ultra-sonication for 20 minutes, followed by the gradual addition of 0.25 M NaOH while stirring, until precipitate ensued or the pH attained 12. The precipitate was filtered, thoroughly washed with deionised water, and subsequently dried in an oven at 70°C for 24 hours. The completed nanocomposite was preserved in an airtight container for subsequent utilisation. This technique guarantees a regulated and repeatable production of high-quality iron oxide/carbon dots nanocomposite.

2.4.4. Synthesis of Fe_3O_4/CD/AgI nanocomposite

The Fe_3O_4/CD/AgI nanocomposite was synthesised using a sequential wet-chemical method under ambient laboratory conditions. Initially, 0.7 g of Fe_3O_4/CD nanoparticles was dispersed in 200 mL of deionised water and sonicated for 20 minutes to obtain a uniform suspension. Next, 0.7 g of the ligand PVP was added to the dispersion and stirred for 15 minutes to promote surface interaction between the nanoparticles and the linker. PVP provides a stable environment for the growth of nanostructures, prevents their aggregation, and controls their size and shape. The heat treatment step facilitates the crystallisation of the nanostructures [32]. Then, 0.4 g of silver nitrate ($AgNO_3$) was introduced while maintaining continuous stirring

and allowed to react for 1 hour to enable coordination of silver ions with PVP. Simultaneously, 0.6 g of potassium iodide (KI) dissolved in 30 mL of deionised water was added dropwise to the mixture under stirring. The reaction was subsequently stirred and gently heated for an additional hour to facilitate the formation and deposition of the Fe_3O_4/CD/AgI nanocomposite. The resulting product was collected by centrifugation, thoroughly washed with deionised water to remove unreacted reagents and by-products, and dried in an oven at 50°C. The final nanocomposite was stored in a desiccator for further characterisation and use in soil remediation experiments.

2.5. Soil sample preparation

Soil samples were collected from the Ibrahim Khalil region, an area of ecological concern due to potential organic contamination. Sampling was conducted at a depth of 0–10 cm, targeting the surface layer most susceptible to atmospheric deposition and anthropogenic influence. Surface debris and litter were carefully removed prior to collection. Approximately 1 kg of soil was obtained using a sterile stainless-steel scoop and immediately placed into pre-cleaned polyethylene bags to minimise contamination and preserve volatile compounds. The soil was air-dried at room temperature, finely ground with a mortar and pestle, and sieved through a 2 mm mesh to achieve uniformity. Prepared samples were stored in sealed, labelled containers under dry conditions until physicochemical characterisation and remediation experiments.

For spiked contamination, 50.0 g of pre-dried, homogenised soil was placed in a glass beaker. A mixture of seven PAHs (final concentration 1.0 mg/L in acetone, 30.0 mL) was evenly sprayed onto the soil while manually stirring to ensure uniform distribution. The soil was then allowed to air-dry at room temperature to evaporate acetone completely. After drying, the soil was thoroughly re-mixed to ensure homogeneity and stored in sterile, airtight containers for subsequent sunlight-driven photodegradation studies.

2.6. Photocatalaytic experiments

2.6.1. Photodegradation of PAHs in contaminated soil

The photocatalytic degradation of PAHs in spiked soil was investigated using Fe_3O_4/CD/AgI nanocomposite. For each experiment, 4.0 g of contaminated soil was combined with 0.1 g of the nanocomposite, corresponding to a catalyst loading of 2.5% w/w. Soil moisture was adjusted to approximately 20% by adding deionised water to simulate natural soil conditions and enhance photocatalytic activity. The mixtures were evenly spread in glass Petri dishes and exposed to natural sunlight for up to 8 hours per day, with the 24- and 48-hour samples representing cumulative sunlight exposure. Samples were collected at predetermined intervals (0, 1, 2, 4, 8, 24, and 48 hours) to monitor degradation progress. Control experiments were conducted in the absence of the photocatalyst, sunlight, or both, to separately evaluate the contributions of each factor to PAH degradation.

2.6.2. Optimisation of photocatalytic degradation conditions

Systematic experiments under natural sunlight were conducted to determine the optimal conditions for photocatalytic degradation of PAHs in contaminated soil. The study focused on three parameters: (i) photocatalyst composition, (ii) catalyst dosage, and (iii) sunlight exposure duration. Four photocatalyst treatments were tested: (1) Fe_3O_4/CD, (2) Fe_3O_4/CD/AgI, (3) Fe_3O_4/CD combined with $Na_2S_2O_8$, and (4) Fe_3O_4/CD/AgI combined with $Na_2S_2O_8$. A control consisting of sunlight and water only was included for comparison. Each treatment was applied to 4 g of PAH-contaminated soil prepared as described previously. Catalyst dosage optimisation was performed with Fe_3O_4/CD/AgI at 100 mg, 200 mg, and 300 mg per 4 g soil, corresponding to 2.5%, 5%, and 7.5% w/w, respectively. The effect of sunlight exposure was assessed by sampling at 0, 1, 2, 3, 4, 8, 24, and 48 hours to determine the optimal irradiation time for maximal degradation. All experiments were conducted in triplicate for statistical reliability. Residual PAH concentrations, extracted from the soil, were analysed by GC–MS and compared to untreated controls to evaluate the effects of photocatalyst composition, dosage, and exposure time on degradation kinetics.

2.7. Extraction of residual PAHs from soil

After sunlight exposure, residual PAHs were recovered from the contaminated soil using ultrasonic-assisted solvent extraction. 4 g of soil sample was exposed to three consecutive extractions, each time 13.3 mL of a mixture of chloromethane and methanol (1:1 v/v) was added to the soil sample and sonicated for 20 min. The combined extracts were centrifuged for 10 min at 3500 rpm to remove suspended solids and the supernatant was collected. The supernatant collected from all three consecutive extractions was concentrated using rotary evaporation under vacuum to a final volume of approximately 1.5 mL. The 1.0 µL of concentrated extracts were analysed using GC-MS to determine the residual PAH concentrations and the photocatalytic degradation efficiency was evaluated based on the time-dependent reduction of the target PAHs. To achieve the highest extraction efficiency of PAH from soil, a mixture of various solvents and their different ratios were tested, including: dichloromethane/acetone (3:1, v/v), dichloromethane/n-hexane (1:1, v/v), dichloromethane/methanol (1:1, v/v), and dichloromethane/1-propanol (3:1, v/v). Dichloromethane/methanol (1:1, v/v) consistently provided the highest extraction efficiency for both low- and high-ring PAHs and was therefore selected for subsequent analyses.

3. Results and discussion

3.1. Characterisation

3.1.1. FTIR analysis

Figure 1(a) presents the FTIR spectra of Fe_3O_4, Fe_3O_4/CD, and Fe_3O_4/CD/AgI, showing absorption bands between 400 and 4000 cm^{-1}. For Fe_3O_4, characteristic Fe–O stretching vibrations of the spinel structure were observed at 593.79 and 453.81 cm^{-1}, while the broad O–H stretching band at 3421.64 cm^{-1} indicated surface hydroxyl groups or adsorbed moisture. A peak at 1164.34 cm^{-1} was attributed to C–O–C stretching. Incorporation of carbon dots (CDs) in Fe_3O_4/CD resulted in shifts in these peaks, reflecting

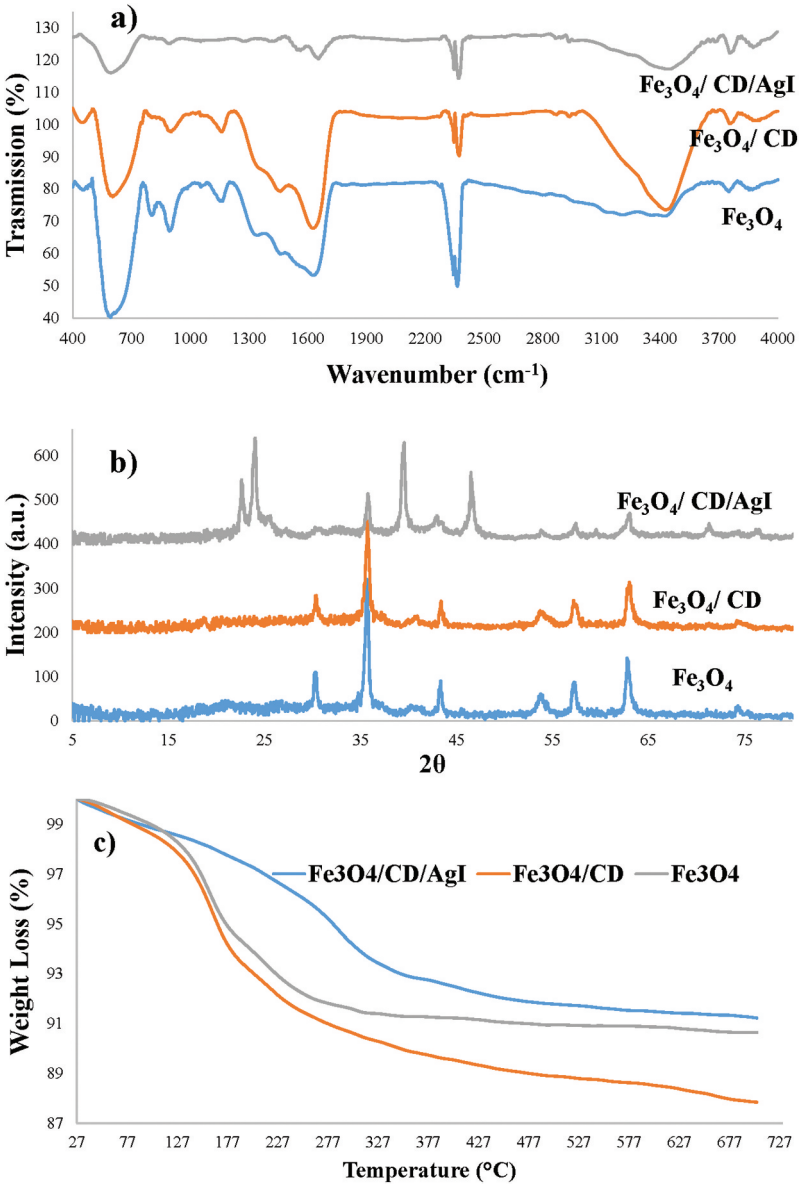

Figure 1. Characterisation of Fe_3O_4, Fe_3O_4/CD, and Fe_3O_4/CD/AgI: (a) FTIR spectra, (b) XRD patterns, and (c) TGA curves.

interactions between Fe_3O_4 and CD surface functional groups [33]. Fe–O vibrations appeared at 604.56 and 447.76 cm^{-1}, and new bands emerged at 1626.06, 1459.37, 1160.87, and 901.86 cm^{-1}, corresponding to C=C, C–O, and C–O–C vibrations. The O–H stretching band shifted slightly to 3426.67 cm^{-1}, confirming retention of hydroxyl groups. These spectral changes indicate effective bonding between Fe_3O_4 and CDs, confirming Fe_3O_4/CD nanocomposite formation [34].

The Fe_3O_4/CD/AgI spectrum showed Fe–O vibrations at 593.02 cm^{-1}, slightly shifted from Fe_3O_4/CD, suggesting modified bonding due to AgI incorporation. The broad O–H band persisted at 3449.15 cm^{-1}, with additional bands at 3754.52 and 3874.55 cm^{-1} (O–H or N–H), likely arising from enhanced hydrogen bonding or surface functionalities introduced during AgI deposition. Although Ag–I bonds are largely IR-inactive, their presence is inferred from shifts in Fe–O vibrations and changes in the overall spectral profile [35], confirming successful integration of AgI into the Fe_3O_4/CD matrix.

3.1.2. XRD analysis

The crystalline structure and phase composition of Fe_3O_4, Fe_3O_4/CD, and Fe_3O_4/CD/AgI nanocomposites were investigated using X-ray diffraction (XRD), as shown in Figure 1(b). The XRD pattern of Fe_3O_4 exhibited sharp and intense diffraction peaks at $2\theta = 30.1°$, 35.5°, 43.2°, 53.4°, 57.0°, and 62.6°, corresponding to the (220), (311), (400), (422), (511), and (440) planes of the face-centred cubic spinel structure of magnetite [36]. The peak at 35.5° was the most prominent, confirming the highly crystalline nature of the Fe_3O_4 nanoparticles. In the Fe_3O_4/CD pattern, these characteristic peaks were retained, indicating that incorporation of carbon dots did not disrupt the spinel lattice. Slight peak broadening and intensity reduction were observed, likely due to decreased crystallite size and induced lattice strain. No distinct peaks were detected for CDs, consistent with their amorphous structure [34].

Upon AgI incorporation, additional peaks appeared at $2\theta \approx 22.6°$, 23.8°, 39.1°, and 46.3°, corresponding to the (100), (002), (110), and (103) planes of hexagonal β-AgI. The coexistence of these AgI reflections with Fe_3O_4 peaks confirms successful formation of the Fe_3O_4/CD/AgI heterostructure. These results indicate that both CDs and AgI were effectively integrated without altering the spinel structure of Fe_3O_4, demonstrating strong structural compatibility. The presence of multiple crystalline phases is expected to enhance charge separation and improve photocatalytic performance under sunlight irradiation.

3.1.3. Thermogravimetric analysis (TGA)

The thermal stability and composition of Fe_3O_4, Fe_3O_4/CD, and Fe_3O_4/CD/AgI nanocomposites were evaluated by thermogravimetric analysis (TGA) in air over the temperature range of 25°C to 700°C (Figure 1(c)). The multi-step weight loss profiles reflect moisture content, decomposition of surface-bound organics, and the thermal behaviour of incorporated components. Fe_3O_4 nanoparticles exhibited excellent thermal stability, with a minor mass loss of 1.34% up to 121.8°C, attributed to the desorption of physically adsorbed water. A subsequent loss of 6.85% between 121.8 and 275.7°C corresponded to the removal of surface hydroxyl groups and possible phase transitions. A final slight decrease of 1.18% at 701.7°C likely resulted from minor structural rearrangements or entrapped volatiles, yielding a total weight loss of 9.37% [37].

Modification with carbon dots (Fe_3O_4/CD) led to increased thermal degradation. The initial 1.83% loss up to 121.1°C was due to water evaporation, followed by a more pronounced 7.39% loss at 286.8°C from decomposition of carbonaceous groups and surface functional groups of CDs. A final loss of 2.95% at 702.2°C, attributed to residual organic decomposition, resulted in an overall weight loss of 12.17%.

The Fe_3O_4/CD/AgI nanocomposite displayed a total mass loss of approximately 9.14%, indicating good thermal stability. The primary loss of 7.06% between 27.4 and 353.1°C was due to removal of adsorbed water and surface-bound organics, while a minor 1.73%

loss at 704.7°C was associated with decomposition of remaining organic components linked to CDs. These results confirm the successful incorporation of carbon dots and AgI into the Fe_3O_4 matrix and demonstrate enhanced decomposition of organic constituents in the hybrid nanocomposites.

3.1.4. Scanning electron microscopy (SEM)

The surface morphology of the synthesised materials was examined using SEM, as shown in Figure 2. The images reveal clear differences in particle structure and aggregation among Fe_3O_4, Fe_3O_4/CD, and Fe_3O_4/CD/AgI nanocomposites, highlighting the effects of each modification step on the catalyst's physical structure. SEM micrographs of Fe_3O_4 nanoparticles (Figure 2(a,b)) show highly aggregated, nearly spherical particles with a dense, bulk-like structure. In contrast, the Fe_3O_4/CD nanocomposite (Figure 2(c,d)) exhibits reduced aggregation and more uniform dispersion, resulting in a porous, less dense morphology that may enhance surface reactivity and facilitate charge transport during photocatalysis. The Fe_3O_4/CD/AgI nanocomposite (Figure 2(e,f)) displays further textural changes, with a rough, granular surface indicating successful decoration of the Fe_3O_4/CD matrix with AgI nanoparticles. This creates a heterogeneous, porous network that can improve light absorption and increase the number of reactive sites available for photocatalytic degradation. Overall, the SEM analysis demonstrates a clear evolution in surface morphology from

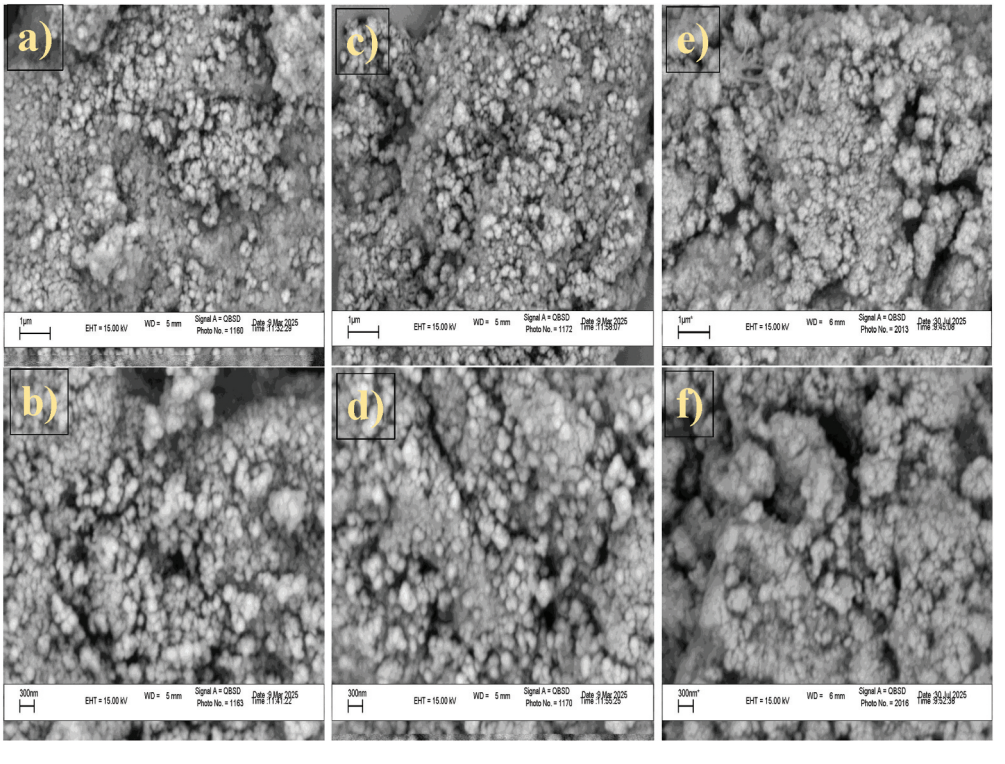

Figure 2. SEM images of Fe_3O_4- based materials: (a, b) Fe_3O_4, (c, d) Fe_3O_4/CD, and (e, f) Fe_3O_4/CD/AgI, showing surface morphology and particle dispersion.

Fe_3O_4 to Fe_3O_4/CD and finally to Fe_3O_4/CD/AgI, confirming the effective stepwise modification of the nanostructure.

3.2. Photocatalytic degradation of PAHs

3.2.1. Influence of sunlight irradiation duration

The effect of sunlight exposure duration on the photocatalytic degradation of seven PAHs–naphthalene, acenaphthylene, phenanthrene, anthracene, fluorene, fluoranthene, and pyrene–was systematically evaluated over 48 hours using Fe_3O_4-based nanocomposites. In all cases, PAH removal increased with irradiation time, showing the most rapid degradation during the first 24 hours, followed by a slower but continuous decline from 24 to 48 hours (Figures 3 and 4). Overall degradation efficiency followed the trend: Fe_3O_4/CD/AgI + PS > Fe_3O_4/CD + PS > Fe_3O_4/CD/AgI > Fe_3O_4/CD.

Naphthalene, the smallest and most volatile PAH with two rings, displayed the highest reactivity. Under Fe_3O_4/CD/AgI + PS, its concentration decreased to 3% after 24 hours and was completely removed by 48 hours (Figure 3(a)). Using Fe_3O_4/CD/AgI or Fe_3O_4/CD + PS, approximately 95% removal was achieved, whereas Fe_3O_4/CD alone left 30% residual, and the sunlight-only control retained 35%. This rapid degradation highlights both the susceptibility of naphthalene to photolysis and the catalytic contribution of radical-generating systems.

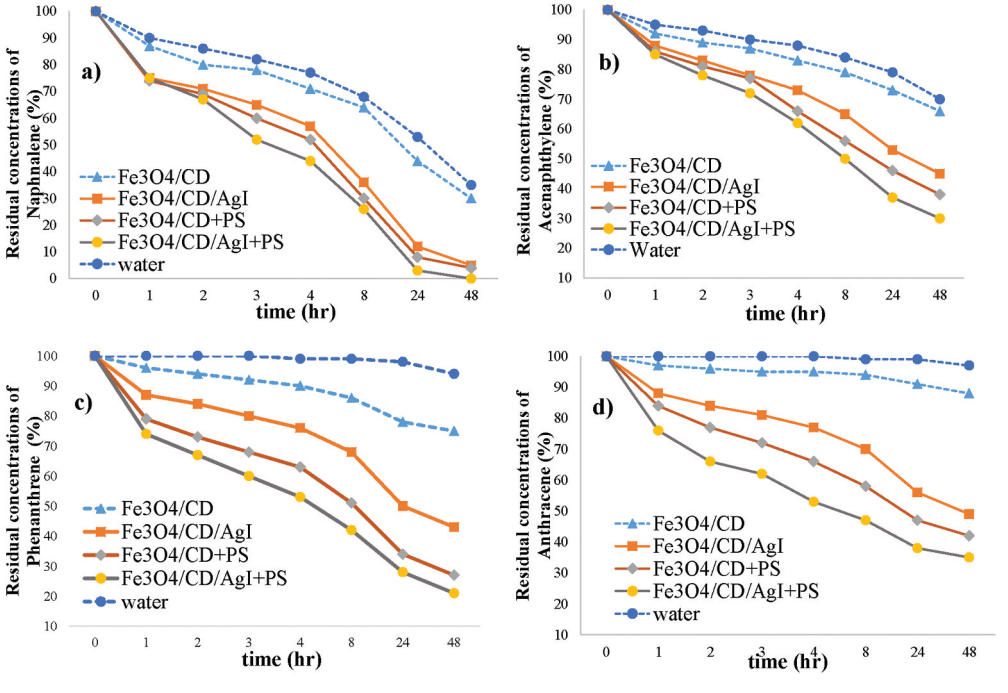

Figure 3. Residual concentrations of (a) naphthalene, (b) acenaphthylene, (c) phenanthrene, and (d) anthracene after sunlight irradiation with Fe_3O_4/CD, Fe_3O_4/CD/AgI, Fe_3O_4/CD + PS, Fe_3O_4/CD/AgI + PS, and water (control).

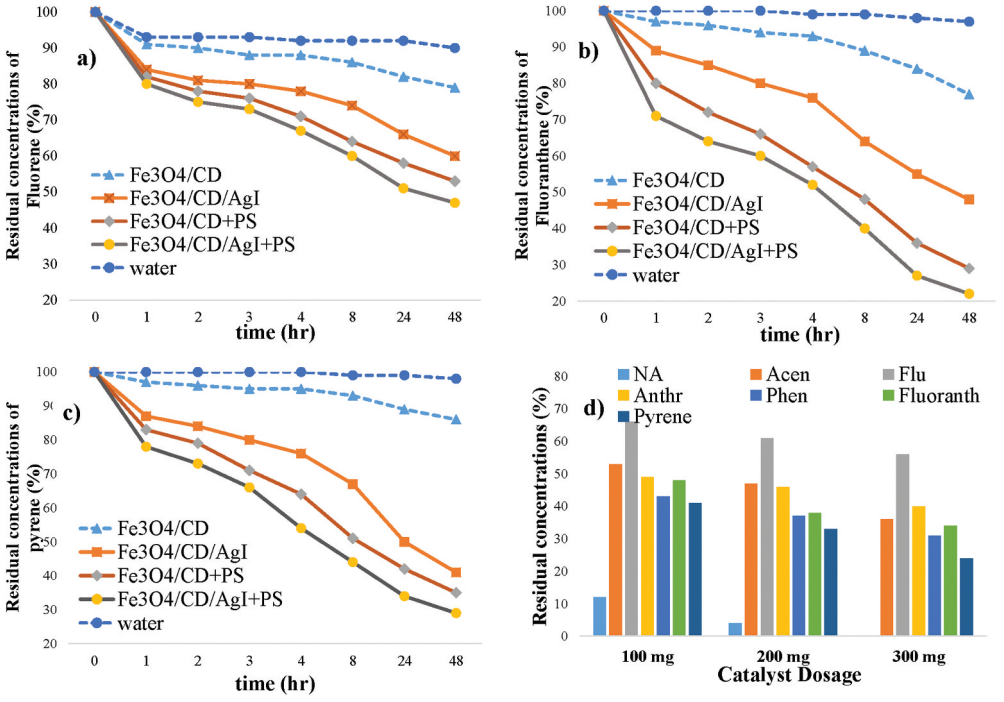

Figure 4. Residual concentrations of (a) fluorene, (b) fluoranthene, (c) pyrene, and (d) effect of catalyst dosage on PAH degradation under sunlight with Fe_3O_4/CD, Fe_3O_4/CD/AgI, Fe_3O_4/CD + PS, Fe_3O_4/CD/AgI + PS, and water (control).

Acenaphthylene (three rings) showed moderate reactivity, reflecting its greater molecular stability compared to naphthalene. Under Fe_3O_4/CD/AgI + PS, its concentration dropped to 30% after 48 hours, while residuals of 66% and 70% were observed with Fe_3O_4/CD and water control, respectively (Figure 3(b)). Most degradation occurred within the first 24 hours, indicating partial susceptibility to oxidative radicals but greater structural resilience than lighter PAHs.

Phenanthrene (three rings, angular structure) exhibited increased resistance due to its compact geometry and strong π–π interactions with soil organic matter. After 48 hours, residual concentrations were 21% with Fe_3O_4/CD/AgI + PS, compared to 75% with Fe_3O_4/CD and 94% under sunlight alone (Figure 3(c)). This slower degradation underscores the critical role of molecular shape in limiting access to reactive species [38].

Anthracene (three rings, linear structure) displayed substantial recalcitrance, with over 88% residual under Fe_3O_4/CD and more than 97% in the control after 48 hours (Figure 3(d)). Although Fe_3O_4/CD/AgI + PS reduced anthracene by 35%, the gradual decline reflects significant adsorption to the soil matrix, limiting its availability for photocatalytic oxidation despite its more open structure relative to phenanthrene.

Fluorene (three rings with a heteroatom bridge) was more labile than anthracene and phenanthrene, likely due to electron density localisation at its bridging position. After 48 hours, Fe_3O_4/CD/AgI + PS reduced fluorene to 47% residual, while Fe_3O_4/CD and water controls retained 79% and 90%, respectively (Figure 4(a)). These results suggest that molecular electronic configuration, in addition to ring count, strongly influences photocatalytic susceptibility.

Fluoranthene (four rings) exhibited moderate resistance but responded efficiently under the optimised system, with residual levels decreasing to 22% using Fe_3O_4/CD/AgI + PS after 48 hours. In contrast, Fe_3O_4/CD and water-only controls preserved 77% and 97%, respectively (Figure 4(b)). The pronounced decrease between 8–24 hours indicates that once adsorption equilibrium was established, radical-mediated oxidation proceeded effectively.

Pyrene (four rings), the most persistent PAH, demonstrated high stability and strong soil adhesion due to extensive aromatic condensation. Its degradation was gradual, with 29% residual under Fe_3O_4/CD/AgI + PS after 48 hours, compared to 86% with Fe_3O_4/CD and 98% in the control (Figure 4(c)). This underscores the requirement for prolonged irradiation to break its condensed π-electron system, confirming pyrene's role as a benchmark for photocatalytic durability [38].

Collectively, these results highlight that PAH degradation is strongly influenced by molecular structure and catalyst composition (Figures 3 and 4). Low-ring PAHs (naphthalene, acenaphthylene) underwent rapid degradation within the first 24 hours, whereas high-ring PAHs (fluoranthene, pyrene) required extended irradiation for substantial removal. The Fe_3O_4/CD/AgI + PS system consistently outperformed other catalysts, benefiting from the synergistic effects of AgI, CDs, and persulphate, which enhance radical generation and maintain robust oxidative pathways [39]. Notably, sunlight exposure shorter than 24 hours was insufficient for effective elimination of resistant PAHs, whereas 48 hours achieved near-complete degradation of both labile and persistent compounds. This operational timeframe demonstrates the practicality of solar-driven soil remediation, emphasising the critical roles of catalyst design and exposure duration in achieving efficient detoxification.

3.2.2. Effect of nanocomposites nature

The photocatalytic performance of the Fe_3O_4-based nanocomposites was strongly influenced by their structural composition. Bare Fe_3O_4 exhibited minimal activity under sunlight, likely due to limited visible-light absorption and rapid electron–hole recombination [40]. Incorporation of carbon dots (CDs) into Fe_3O_4/CD slightly improved degradation efficiency, attributable to enhanced visible-light absorption and superior electron transport. CDs act as electron reservoirs, reducing charge recombination and facilitating photocatalytic reactions [25].

Further addition of AgI to the Fe_3O_4/CD matrix significantly enhanced photocatalytic efficiency. AgI, a visible-light-responsive semiconductor, interacts closely with the Fe_3O_4/CD composite, promoting effective separation of photogenerated electrons and holes and extending light absorption into the visible range. This improved charge separation increases the production of reactive oxygen species (ROS), which are essential for PAH degradation [24].

As shown in the PAH degradation profiles (Figures 3 and 4), both Fe_3O_4/CD and Fe_3O_4/CD/AgI exhibited superior activity compared to bare Fe_3O_4; however, neither achieved complete degradation of all PAHs within 48 hours. Nevertheless, the inclusion of AgI markedly enhanced removal of mid- to high-molecular-weight PAHs relative to Fe_3O_4/CD alone, highlighting the beneficial role of AgI in targeting more persistent pollutants.

3.2.3. Enhancement due to $Na_2S_2O_8$ addition

The addition of sodium persulphate ($Na_2S_2O_8$) to the photocatalytic system markedly enhanced the degradation of all seven PAHs, particularly those with higher molecular weight and condensed aromatic rings [41]. When incorporated into Fe_3O_4/CD and Fe_3O_4/CD/AgI composites, persulphate acted as a strong oxidising agent, generating reactive sulphate radicals (SO_4•$^-$) through photolytic activation and catalytic interaction with the composite surface under sunlight. Unlike hydroxyl radicals (•OH), which are highly reactive but non-selective, sulphate radicals possess higher redox potential and greater selectivity towards electron-rich aromatic compounds, enabling more efficient attack on stable PAH molecules and enhancing mineralisation.

Additionally, SO_4•$^-$ radicals exhibit extended lifetimes in aqueous and humid soil environments, allowing deeper penetration and sustained oxidation activity [42]. Comparative experiments demonstrated that inclusion of $Na_2S_2O_8$ accelerated degradation rates and increased overall removal efficiency, particularly during the later stages of solar exposure (24–48 h). Persistent PAHs such as anthracene and fluoranthene, which degraded slowly without oxidant support, showed significantly improved elimination in the presence of persulphate.

In the Fe_3O_4/CD/AgI + PS system, the combination of visible-light photocatalysis and persulphate activation created a highly oxidative environment, producing multiple reactive oxygen species (ROS), including SO_4•$^-$, •OH, and superoxide radicals (O_2•$^-$) [43]. This multi-pathway oxidation facilitated near-complete removal of low-molecular-weight PAHs and substantial degradation of high-molecular-weight PAHs within 48 hours, as reflected in the individual PAH degradation profiles (Figures 3 and 4).

3.2.4. Control (sunlight-only) performance

Control experiments were conducted to assess the effect of direct photolysis on PAH-contaminated soil, where samples were treated only with water and exposed to natural sunlight for 48 hours. The results revealed minimal degradation, with most PAHs retaining over 90% of their initial concentrations. Specifically, levels after 48 hours were: naphthalene 35%, acenaphthylene 70%, phenanthrene 94%, anthracene 97%, fluorene 90%, fluoranthene 97%, and pyrene 98% (Figures 3 and 4). The limited photolytic activity under sunlight is likely due to the low quantum efficiency of direct PAH photodegradation in soil matrices, as well as the protective effect of soil particles, which attenuate UV penetration [44]. Additionally, the intrinsic stability of high-molecular-weight PAHs further impedes their breakdown in the absence of catalytic assistance [45]. These findings indicate that natural sunlight alone is insufficient for effective PAH remediation in contaminated soils and underscore the crucial role of photocatalyst-mediated and radical-driven processes in achieving substantial degradation.

3.2.5. Influence of catalyst dosage on PAHs degradation

The effect of Fe_3O_4/CD/AgI catalyst loading on the photocatalytic degradation of seven PAHs was investigated at 100 mg, 200 mg, and 300 mg per 4 g of contaminated soil (corresponding to 2.5%, 5%, and 7.5% w/w, respectively). After 48 hours of sunlight exposure, residual PAH concentrations decreased with increasing catalyst dosage. At 100 mg, heavier PAHs such as phenanthrene (45%), anthracene (48%), and pyrene

(42%) showed limited degradation, whereas lighter PAHs like naphthalene were more effectively removed (12%). Increasing the dosage to 200 mg significantly enhanced degradation for all PAHs, reducing naphthalene to 4% and pyrene to 33%. At 300 mg, slight additional reductions were observed, with phenanthrene, anthracene, and pyrene residuals decreasing to 33%, 42%, and 25%, respectively, and complete elimination of naphthalene (0%).

The marginal improvement from 200 mg to 300 mg likely results from catalyst aggregation and increased light scattering at higher loadings, which reduce the photocatalytically active surface area [46]. These results indicate that 200 mg (5% w/w) represents the optimal dosage, balancing efficient degradation with catalyst utilisation. This loading effectively removes both low- and high-molecular-weight PAHs, demonstrating the practical applicability of Fe_3O_4/CD/AgI nanocomposites for solar-driven soil remediation. The dosage-dependent trends are summarised in Figure 4(d).

3.3. Comparative efficiency for individual PAHs

The overall photocatalytic degradation efficiency of the seven PAHs followed the order: naphthalene > acenaphthylene > fluorene > fluoranthene > anthracene > phenanthrene > pyrene (Figures 3 and 4). Low-molecular-weight PAHs with fewer aromatic rings, such as naphthalene and acenaphthylene, degraded more rapidly due to higher aqueous solubility, lower molecular stability, and weaker adsorption to the soil matrix. In contrast, high-ring PAHs, including pyrene and anthracene, exhibited greater resistance to degradation, reflecting their enhanced molecular stability, pronounced hydrophobicity, and strong affinity for soil organic matter, which limit their bioavailability and accessibility to reactive species [47].

In the most effective system, Fe_3O_4/CD/AgI + PS, pyrene retained only 29% of its initial concentration after 48 hours, whereas in the Fe_3O_4/CD system alone, 86% remained undegraded. This pronounced difference highlights the critical influence of molecular structure and catalyst composition on degradation efficiency. These results emphasise the importance of tailoring remediation strategies to the specific PAH profile of contaminated sites, considering both the reactivity of individual compounds and the design of the photocatalyst.

The observed differences in degradation efficiencies are further influenced by PAH speciation and initial content in the soil. The investigated PAHs included low-molecular-weight compounds (naphthalene, acenaphthylene, fluorene) and high-molecular-weight compounds (phenanthrene, anthracene, fluoranthene, pyrene), which differ markedly in physicochemical properties and soil interactions. Low-molecular-weight PAHs exhibited higher bioavailability and faster degradation, whereas high-molecular-weight PAHs showed increased persistence due to strong sorption to the loamy soil matrix, resulting in reduced accessibility to reactive species. These speciation-dependent characteristics explain the degradation trends observed with the Fe_3O_4/CD/AgI nanocomposite under realistic soil conditions [4,48–50].

3.4. Mechanistic insights

The purpose of the radical quenching studies was to investigate the amount of reactive species involved in the photo-degradation of pyrene over Fe_3O_4/CD/AgI + PS. In order to do

this, 10 m mol solutions of benzoquinone (BQ), tert-butanol (TBA), and methanol (MeOH) were added to photocatalytic experiments as scavengers to trap O_2, OH, and $SO_4^{\bullet-}$, respectively [51,52]. Figure 5 illustrates how the removal rate of pyrene photodegradation in the presence of BQ, TBA, and MeOH dropped by 26%, 34%, and 45%, respectively, in comparison to the no quencher (CK). Because of this, the inhibition sequence is MeOH > TBA > BQ, suggesting that $SO_4^{\bullet-}$ was primarily responsible for the photocatalytic degradation of PAHs on Fe_3O_4/CD/AgI + PS. Nevertheless, •OH and O2•$^{-}$ radicals also had a significant impact on the PAH degradation process.

Figure 6 illustrates the photocatalytic probable mechanism of the Z-scheme AgI/Fe_3O_4/CD hetero-nanostructure. Based on the aforementioned analysis, test results, and literature. AgI's band gap is 2.8 eV, and its ECB and EVB reach −0.42 eV and 2.38 eV, respectively, in accordance with current research investigations. Furthermore, Fe_3O_4's ECB and EVB are −0.58 eV and 0.99 eV, respectively, and its band gap is 1.57 eV [53]. Electrons in the AgI and Fe_3O_4 components of the AgI/Fe_3O_4/CD nanocomposite are excited from the VB to the CB by visible light exposure. AgI, CD, and Fe_3O_4 interacted closely, resulting in the formation of an interface based on a corresponding energy level structure. The adsorbed O_2 on the composite surface absorbed the photogenerated electrons in the CB of AgI and Fe_3O_4, and the resulting •O_2- (E0 (•O_2/O2) = ~0.33 V/NHE) was an efficient active material to break down organic contaminants [53]. Furthermore, the transferred electrons on the CB of Fe3O4 and AgI can react with adsorbed O2 to form H2O2 molecules since the E0 of O2/H2O2 against NHE is +0.682 eV [52]. •OH is then produced when the electron-rich Fe-centers of Fe3O4 combine with the produced H2O2 molecules, activating the HO−OH link [54]. Furthermore, the photogenerated electrons were preserved in the more negative Fe3O4 CB while the photogenerated hole was preserved within the more positive VB of AgI. Furthermore, AgI's VB (2.38 V) was more positive

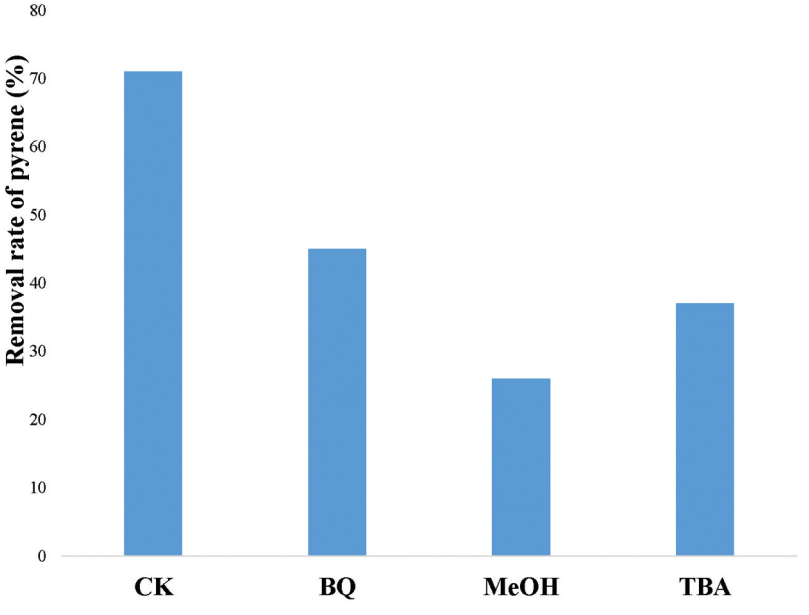

Figure 5. The removal percentage of pyrene using Fe_3O_4/CD/AgI +PS in presence of three types of radical quencher.

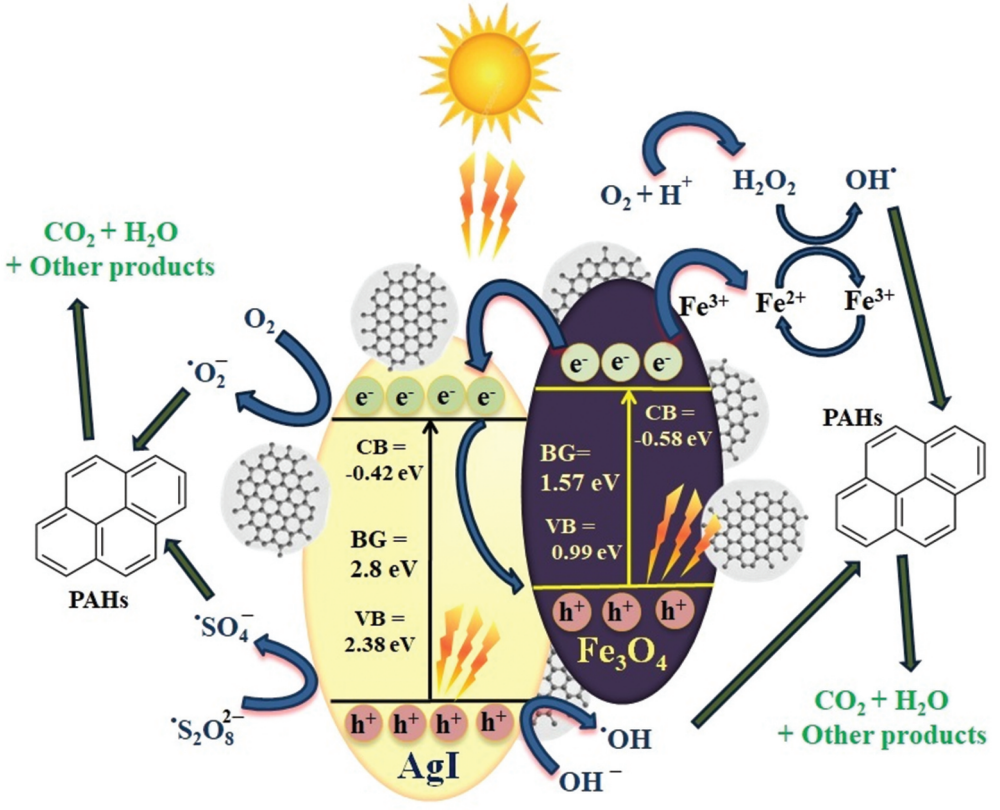

Figure 6. The photocatalytic mechanism of Fe_3O_4/CD/AgI + PS under sun-light irradiation.

than that of •OH/OH^- (1.99 V) and SO4•−/S2O8-2 (SO4•−/S2O8-2 = 2.10 V), indicating that the holes can either directly oxidise pollutants or react with H2O and S2O8-2 to produce •OH and SO4•−, respectively [53]. Improved photocatalytic capabilities can arise from increased light absorption and increased charge carrier mobility caused by the presence of CD nanostructures in the nanocomposite composition. These factors led to a significant increase in the photocatalytic activity for degrading the organic pollutant, and the Z-scheme AgI/Fe3O4/C hetero-nanostructure could significantly speed up the photocatalytic breakdown of the PAH molecules.

3.5. Degradation pathway of PAHs by the Fe_3O_4/CD/AgI system

The degradation products of the seven spiked PAHs, identified by GC–MS, are summarised in Figure 7. The oxidative transformation of PAHs by the Fe_3O_4/CD/AgI system can be described in three main stages, as inferred from the detected intermediates and relevant literature [55]. In the initial stage, reactive oxygen species (ROS) attack the aromatic rings, generating quinonoid and phenolic derivatives [56]. Representative products at this stage included 9,10-anthracenedione, a characteristic quinone of high-molecular-weight PAHs, and 2,4-di-tert-butylphenol, indicative of hydroxylation and alkyl-

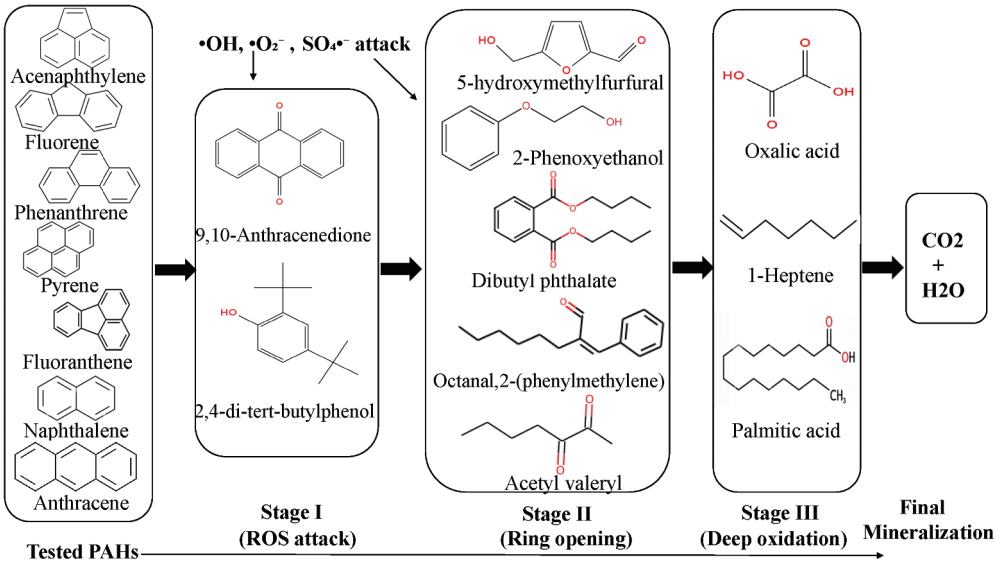

Figure 7. Proposed photocatalytic degradation pathway of seven PAHs under Fe_3O_4/CD/AgI systems.

substitution reactions. These transformations disrupt the conjugated π-system, facilitating subsequent ring cleavage [57].

During the second stage, the oxidised intermediates undergo ring-opening reactions, yielding oxygenised fragments. The detection of dibutyl phthalate suggests the involvement of phthalic acid intermediates, esterified via radical coupling with alkyl groups derived from the soil matrix [57]. Additional ring-cleavage products, such as 5-hydroxymethylfurfural, ethanol, 2-phenoxy, and octanal,2-(phenylmethylene), confirm the conversion of aromatic structures into furanic, benzylic alcohol, and aldehydic derivatives. The appearance of acetyl valeryl indicates further oxidative cleavage of opened-ring intermediates into medium-chain ketones.

In the final stage, persistent ROS progressively decompose these oxygenised intermediates into small organic acids and hydrocarbons. Oxalic acid was identified as a stable end-product of aromatic oxidation, while 1-heptene reflects decarboxylative fragmentation of aliphatic chains. The presence of palmitic acid suggests the transient formation of long-chain fatty acid-like species, which are gradually degraded under oxidative conditions. Ultimately, these intermediates are mineralised to CO_2 and H_2O, completing the degradation process [52,54].

3.6. Comparison with previous studies

The sunlight-driven photocatalytic degradation of PAHs in soil presented in this study offers distinct advantages over previously reported approaches, which predominantly rely on UV irradiation or aqueous-phase treatment. Traditional UV-based photocatalytic systems generally require energy-intensive artificial light sources and often employ hazardous oxidants such as hydrogen peroxide or ozone, limiting their sustainability and practical applicability [58]. In contrast, the present system achieved complete removal

Table 1. Comparison of the current study with other reported related research.

Catalyst	Target PAHs	Light source/ Time	PAH Degradation %/Metrics	Ref.
Akaganeite(β-FeOOH) nanorods	Phenanthrene	UV, ~96 h2	Phenanthrene: ~100% degraded, in soil	[55]
TiO_2 (0.5%)	Phenanthrene, Pyrene, BaP	UV, prolonged hours	Phenanthrene 75%; Pyrene ~70%; BaP ~72%, in soil	[60]
α-FeOOH, β-FeOOH,Fe_3O_4, γ-Fe_2O_3, and αFe_2O_3+oxalic acid	Benzo[a]pyrene	UV, ~120 h	95–100% degradation achieved, in soil	[61]
TiO_2	Acenaphthene,Anthracene, Benzo[a]anthracene, Indene [1,2,3 cd]pyrene,Dibenzo[ah] anthracene, Benzo[ghi]pyrene	UV, ~12 h	Acenaphthene:91%; Anthracene:84%; Benzo[a] anthracene: 75%; Indene [1,2,3-cd]pyrene: 67%; Dibenzo[ah]anthracene:62%; Benzo[ghi]pyrene: 59%, in mangrove sediment, soil	[62]
Nano-TiO_2	Total PAHs, HMW PAHs	UV, 1 h	Total PAHs: ~93%; HMW PAHs: ~94–95%, on biochar	[63]
Fe_3O_4/CDs/AgI +PS	Naphthalene, Fluoranthene, Pyrene, Acenaphthylene, Phenanthrene, Anthracene, Fluorene	Natural sunlight, 48 hours	Naphthalene:100%, Fluoranthene:78%, Pyrene71%, Acenaphthylene:70%, Phenanthrene: 79%, Anthracene: 65%, Fluorene: 53%,in soil	This study

of naphthalene and over 70% degradation of fluoranthene and pyrene under natural sunlight, without the need for additional energy input or toxic chemicals. Furthermore, the incorporation of carbon dots and AgI enhanced visible-light absorption and promoted efficient charge separation, resulting in superior degradation performance relative to bare Fe_3O_4 or other conventional photocatalysts [59]. These results highlight the feasibility of harnessing solar energy for soil remediation, providing an economical and environmentally friendly alternative to conventional methods. Compared to commonly used photocatalysts such as TiO_2 that mentioned in Table 1 [55,60–63] and other conventional materials, the Fe_3O_4/CD/AgI composite offers several advantages: all precursors are derived from industrial and agricultural waste, making the catalyst cost-effective and environmentally sustainable. The combination of carbon dots and AgI extends light absorption into the visible region, enabling efficient sunlight utilisation rather than relying on energy-intensive UV lamps [59]. Furthermore, the catalyst demonstrates breakthrough performance for recalcitrant PAHs such as pyrene, achieving 71% degradation under natural sunlight within 48 h, which is comparable to or exceeds many TiO_2-based systems under UV irradiation [60,62]. A comparative summary with other published studies is presented in Table 1.

3.7. Practical application potential, limitations, and future perspectives

The developed Fe_3O_4/CD/AgI nanocomposite was investigated for practical potential soil remediation applications due to its efficient sunlight-driven photocatalytic activity, magnetic recoverability, and sustainable material design. Importantly, all degradation

experiments were conducted using real soil rather than artificial matrices, enhancing the environmental relevance of the obtained results. The investigated soil was classified as loamy soil, with a measured pH of 7.5 and an organic matter content of 1.2%, representing realistic soil conditions. Although the present study confirmed effective PAH degradation under loamy soil conditions, variations in soil composition such as pH, organic matter, and texture, may influence photocatalytic efficiency, highlighting the need for broader validation across different soil types and contamination scenarios [64]. Soil properties such as pH, organic matter content, and texture can affect pollutant adsorption, radical scavenging behaviour, and mass transfer processes. In this work, the magnetic separation performance of the catalyst was experimentally verified and demonstrated effective recovery from the soil matrix; however, catalyst reuse over multiple degradation cycles was not investigated. Future studies should therefore include systematic reusability and stability assessments following repeated magnetic recovery, as emphasised in previous investigations of magnetic photocatalysts [64,65].

From a materials design perspective, the development of the Fe_3O_4/CD/AgI nanocomposite followed a stepwise optimisation strategy. Initially, Fe_3O_4/carbon dots were synthesised to enhance degradation rates through improved visible-light absorption and charge transfer. Subsequently, AgI was incorporated to further extend visible-light responsiveness and suppress charge recombination. Finally, persulphate activation was introduced to amplify reactive oxygen species generation and maximise degradation efficiency. This synergistic combination maximises photocatalytic performance. From an economic standpoint, the utilisation of waste-derived precursors, solar-driven operation, and magnetic recovery suggests potential cost reductions compared to conventional UV-driven or chemically intensive remediation technologies [64,66].

In terms of environmental safety, the incorporation of silver-containing components introduces potential ecological concerns related to metal leaching and long-term persistence in soil environments. Although no adverse effects were observed during the short-term experiments conducted in this work, comprehensive eco-toxicological assessments–including impacts on soil microorganisms and plants–are necessary prior to field-scale application, as highlighted in previous studies on silver-based nanomaterials [67].

3.8. Environmental and practical implications

The synthesis of photocatalysts from waste-derived precursors, namely iron waste and wheat straw, aligns with circular economy principles by transforming industrial and agricultural byproducts into valuable functional materials [68]. The Fe_3O_4/CD/AgI + PS system demonstrated high photocatalytic performance under natural sunlight, while offering magnetic recoverability and utilising non-toxic components, underscoring its potential for passive or semi-passive field-scale remediation of PAH-contaminated soils. This approach reduces reliance on artificial energy inputs and minimises secondary pollution, making it both environmentally and economically sustainable. Although soil parameters such as organic matter content, moisture, and texture were not directly evaluated in this study, they are known to

influence PAH bioavailability and photocatalytic efficiency under field conditions [19], potentially affecting interactions among contaminants, catalysts, and reactive species.

4. Conclusion

This study establishes a highly effective and sustainable photocatalytic system using Fe_3O_4/CD/AgI nanocomposites, synthesised entirely from iron waste and agricultural biomass. The ternary nanocomposite demonstrated exceptional photocatalytic performance under natural sunlight, particularly in the presence of sodium persulphate, achieving near-complete degradation of both low- and high-molecular-weight PAHs in contaminated soils. The outstanding efficacy arises from the synergistic interplay among Fe_3O_4, carbon dots, and AgI, which collectively enhance visible-light absorption, facilitate efficient charge separation, and generate abundant reactive oxygen species. Beyond its high degradation efficiency, the system offers magnetic recoverability, green and waste-derived synthesis, and reliance on solar energy, making it uniquely suitable for scalable, field-applicable soil remediation. By combining circular economy principles with cutting-edge photocatalysis, this approach represents a paradigm shift towards environmentally responsible and cost-effective remediation of persistent organic pollutants. The green synthesis of the Fe_3O_4/CD/AgI nanocomposite not only utilises waste materials but also contributes to reducing carbon emissions and lowering reliance on primary mineral extraction, enhancing its overall environmental sustainability. Considering life cycle impacts, this strategy represents a practical example of eco-friendly material design that supports sustainable soil remediation technologies in line with contemporary environmental and societal priorities [69,70]. Future investigations should expand the evaluation across diverse soil types and real-world contamination scenarios to fully unlock its potential for broad environmental applications, paving the way for practical deployment of solar-driven, sustainable soil remediation technologies.

Disclosure statement

No potential conflict of interest was reported by the author(s).

Acknowledgments

The authors gratefully acknowledge the financial support provided by the University of Zakho for this work.

References

[1] Y. Gao, Y. Xue, J. Ji, K. Zhen, X. Tang, P. Zhang, C. Wang and H. Sun, Chemosphere **313**, 137450 (2023). doi:10.1016/j.chemosphere.2022.137450

[2] Y. Gao, F. Yang, H. Jian, K. Zhen, P. Zhang, X. Tang, Z. Fu, W. Xu, C. Wang and H. Sun, J. Environ. Chem. Eng. **9** (6), 106733 (2021). doi:10.1016/j.jece.2021.106733

[3] X. Hu, Z. Yu, L. Chen, Y. Huang, C. Zhang, F. Salehi, R. Chen, R.M. Harrison and J. Xu, Combust. Flame. **236**, 111760 (2022). doi:10.1016/j.combustflame.2021.111760
[4] M. Emre, J.V. Tongco, R. Permana and R. Permana, Aquat. Soil Pollut. **4** (2), 111 (2024). doi:10.53623/tasp.v4i2.490
[5] N. Premnath, K. Mohanrasu, R.G.R. Rao, G.H. Dinesh, G.S. Prakash, V. Ananthi, K. Ponnuchamy, G. Muthusamy and A. Arun, Chemosphere **280**, 130608 (2021). doi:10.1016/j.chemosphere.2021.130608
[6] M.U. Ali, L. Siyi, B. Yousaf, Q. Abbas, R. Hameed, C. Zheng, X. Kuang and M.H. Wong, Crit. Rev. Environ. Sci. Technol. **51** (9), 857 (2021). doi:10.1080/10643389.2020.1738854
[7] S. Li, Z. Jiang and S. Wei, Environ. Res. **263**, 120035 (2024). doi:10.1016/j.envres.2024.120035
[8] I.C. Ossai, A. Ahmed, A. Hassan and F.S. Hamid, Environ. Technol. Innov. **17**, 100526 (2020). doi:10.1016/j.eti.2019.100526
[9] B. Bukowska, K. Mokra and J. Michałowicz, Int. J. Mol. Sci. **23** (11), 6348 (2022). doi:10.3390/ijms23116348
[10] E. Drwal, A. Rak and E.L. Gregoraszczuk, Toxicology **411**, 133 (2019). doi:10.1016/j.tox.2018.10.003
[11] X. Liu, J. Huang, C. Song, T. Zhang, Y. Liu and L. Yu, Hum. Exp. Toxicol. **42**, 09603271231191436 (2023). doi:10.1177/09603271231191436
[12] S.R. Wild and K.C. Jones, Environ. Pollut. **88** (91), 91–108 (1995). doi:10.1016/0269-7491(95)91052-M
[13] A.B. Patel, S. Shaikh, K.R. Jain, C. Desai and D. Madamwar, Front. Microbiol. **11**, 562813 (2020). doi:10.3389/fmicb.2020.562813
[14] J. Liu, L. Zhao, Q. Liu, J. Li, Z. Qiao, P. Sun and Y. Yang, Int. J. Environ. Sci. Technol. **19** (1), 601–624 (2022). doi:10.1007/s13762-021-03144-1
[15] Q. Wang, S. Guo, M. Ali, X. Song, Z. Tang, Z. Zhang, M. Zhang and Y. Luo, J. Hazard. Mater. **433**, 128749 (2022). doi:10.1016/j.jhazmat.2022.128749
[16] G. Devendrapandi, X. Liu, R. Balu, R. Ayyamperumal, M.V. Arasu, M. Lavanya, V.R.M. Reddy, W. K. Kim and P.C. Karthika, Environ. Res. **249**, 118404 (2024). doi:10.1016/j.envres.2024.118404
[17] A.S. Ganie, S. Bano, N. Khan, S. Sultana, Z. Rehman, M.M. Rahman, S. Sabir, F. Coulon and M. Z. Khan, Chemosphere **275**, 130065 (2021). doi:10.1016/j.chemosphere.2021.130065
[18] C. Huang, C. Zhang, D. Huang, D. Wang, S. Tian, R. Wang, Y. Yang, W. Wang and F. Qin, Chem. Eng. J. **404**, 127066 (2021). doi:10.1016/j.cej.2020.127066
[19] M. Mazarji, T. Minkina, S. Sushkova, S. Mandzhieva, G.N. Bidhendi, A. Barakhov and A. Bhatnagar, J. Environ. Manage. **284**, 112023 (2021). doi:10.1016/j.jenvman.2021.112023
[20] S. Peiris, H.B. de Silva, K.N. Ranasinghe, S.V. Bandara and I.R. Perera, J. Chin. Chem. Soc. **68** (5), 738 (2021). doi:10.1002/jccs.202000465
[21] Y. Sang, H. Liu and A. Umar, ChemCatchem. **7** (4), 559 (2015). doi:10.1002/cctc.201402812
[22] S. Navalon, A. Dhakshinamoorthy, M. Alvaro and H. Garcia, Chem. Rev. **114** (12), 6179 (2014). doi:10.1021/cr4007347
[23] A.N. Garcia, Y. Zhang, S. Ghoshal, F. He and D.M. O'Carroll, Environ. Sci. Technol. **55** (13), 8464 (2021). doi:10.1021/acs.est.1c01251
[24] M. Liu, Y. Ye, J. Ye, T. Gao, D. Wang, G. Chen and Z. Song, Magnetochemistry **9** (4), 110 (2023). doi:10.3390/magnetochemistry9040110
[25] B. Yang, Y. Yu, H. Liu, L. Yang, Z. Hua, Y. Feng and L. Xue, ACS Omega **8** (1), 718 (2022). doi:10.1021/acsomega.2c05979
[26] Y.-Y. Yang, C.-G. Niu, X.-J. Wen, L. Zhang, C. Liang, H. Guo, D.-L. Guan, H.-Y. Liu and G.-M. Zeng, J. Colloid. Interface Sci. **533**, 636 (2019). doi:10.1016/j.jcis.2018.09.008
[27] H. Yu, L. Liu, X. Wang, P. Wang, J. Yu and Y. Wang, Trans. **41** (34), 10405 (2012). doi:10.1039/C2DT30864A
[28] A. Akhundi and A. Habibi-Yangjeh, Mater. Chem. Phys. **174**, 59 (2016). doi:10.1016/j.matchemphys.2016.02.052
[29] N.U.M. Nizam, M.M. Hanafiah and K.S. Woon, Nanomaterials **11** (12), 3324 (2021). doi:10.3390/nano11123324

[30] A.I. Osman, Y. Zhang, M. Farghali, A.K. Rashwan, A.S. Eltaweil, E.M. Abd El-Monaem, I.M. A. Mohamed, M.M. Badr, I. Ihara, D.W. Rooney and P.-S. Yap, Environ. Chem. Lett. **22** (2), 841 (2024). doi:10.1007/s10311-023-01682-3
[31] A. Biswas, A.K. Patra, S. Sarkar, D. Das, D. Chattopadhyay and S. De, Eng. Asp. **589**, 124420 (2020). doi:10.1016/j.colsurfa.2020.124420
[32] N.M. Al-Hada, S. Xu, A.M. Al-Ghaili, B.A. Al-Asbahi, H. Baqiah, J. Yang, M.N. Azlan and Q. Li, Results Phys. **65**, 107990 (2024). doi:10.1016/j.rinp.2024.107990
[33] S. Altaf, R. Zafar, W.Q. Zaman, S. Ahmad, K. Yaqoob, A. Syed, A.J. Khan, M. Bilal and M. Arshad, Environ. Saf. **226**, 112826 (2021). doi:10.1016/j.ecoenv.2021.112826
[34] A. Jiananda, E.K. Sari, D.A. Larasati, R.M. Tumbelaka, H. Ardiyanti, M.Y. Darmawan, N. I. Istiqomah, S.T. Wicaksono, E. Suharyadi and E. Suharyadi, Carbon Trends. **13**, 100305 (2023). doi:10.1016/j.cartre.2023.100305
[35] G.U. Rehman, M. Tahir, P.S. Goh, A.F. Ismail and I.U. Khan, Powder. Technol. **356**, 547 (2019). doi:10.1016/j.powtec.2019.08.026
[36] Z.I. Takai, M.K. Mustafa, S. Asman and K.A. Sekak, Int. J. Nanoelectron. Mater. **618** (24), (2019). doi:10.4028/j.nanoelemat2019.618.24
[37] I.J. Biosci, A.K. Bhuiya, A. Rahman and S.A. Islam, Int. J. Biosci. **6655**, 123 (2023). doi:10.12692/ijb/22.6.123-132
[38] K. Sohara, K. Yamauchi, X. Sun, K. Misawa and Y. Sekine, Catalysts **11** (3), 400 (2021). doi:10.3390/catal11030400
[39] Y. Yan, Z. Wei, X. Duan, M. Long, R. Spinney, D.D. Dionysiou, R. Xiao and P.J.J. Alvarez, Environ. Sci. Technol. **57** (33), 12153 (2023). doi:10.1021/acs.est.3c05153
[40] S. Kumar, S. T, B. Kumar, A. Baruah and V. Shanker, J. Phys. Chem. C. **117** (49), 26135 (2013). doi:10.1021/jp409651g
[41] S.A. Mokhtari, M. Gholami, A. Dargahi and M. Vosoughi, Water. Treat. **213**, 311 (2021). doi:10.5004/dwt.2021.26716
[42] R. Xiao, Z. Luo, Z. Wei, S. Luo, R. Spinney, W. Yang and D.D. Dionysiou, Curr. Opin. Chem. Eng. **19**, 51 (2018). doi:10.1016/j.coche.2017.12.005
[43] R. Luo, C. Wang, Y. Yao, J. Qi and J. Li, Environ. Sci. Water. Res. Technol. **8** (3), 465 (2022). doi:10.1039/D1EW00731A
[44] G. Eker and M. Hatipoglu, Environ. Technol. **44** (28), 3793 (2019). doi:10.1080/09593330.2018.1491635
[45] Y. Wang, H. Tian, C. Zhang, J. Xu, X. Liu, F. Ma, X. Wei and Y. Sun, Sci. Total Environ. **931**, 172768 (2024). doi:10.1016/j.scitotenv.2024.172768
[46] J. Melcher, N. Barth, C. Schilde, A. Kwade and D. Bahnemann, J. Mater. Sci. **52** (2), 1047 (2017). doi:10.1007/s10853-016-0400-z
[47] M. Altarawneh and L. Ali, Energyamp; Fuels. **38** (22), 21735 (2024). doi:10.1021/acs.energyfuels.4c03513
[48] H. Cheng, Q. Sun, Y. Bian, J. Han, X. Jiang, J. Xue and Y. Song, Sci. Total Environ. **930**, 172802 (2024). doi:10.1016/j.scitotenv.2024.172802
[49] A. Ukalska-Jaruga and B. Smreczak, Molecules **25** (11), 2470 (2020). doi:10.3390/molecules25112470
[50] D. Li, P. Su, M. Tang and G. Zhang, Environ. Saf. **266**, 115589 (2023). doi:10.1016/j.ecoenv.2023.115589
[51] L. Wu, Y. Gao, S. Qiu, Z. Hu, C. Liu, C. Yue and J. Zhou, Chemosphere **368**, 143699 (2024). doi:10.1016/j.chemosphere.2024.143699
[52] A. Khodayari and S. Sohrabnezhad, J. Solid State Chem. **297**, 122087 (2021). doi:10.1016/j.jssc.2021.122087
[53] Y. Xie, Y. Sun, J. Ge, W. Chen, Y. Zheng and P. Rao, New J. Chem. **46** (23), 11437 (2022). doi:10.1039/D2NJ01359B
[54] A. Shrivastava, U. Kumar and I. Sinha, Ind. Eng. Chem. Res. **63** (36), 15721 (2024). doi:10.1021/acs.iecr.4c01386
[55] H. Gupta, RSC Adv. **6** (114), 112721 (2016). doi:10.1039/C6RA24602H

[56] H.-Y. Ma, L. Zhao, L.-H. Guo, H. Zhang, F.-J. Chen and W.-C. Yu, J. Hazard. Mater. **369**, 719 (2019). doi:10.1016/j.jhazmat.2019.02.080
[57] J. Zhou, Y. Tian, C. Yan, D. Li, T. Liu, G. Liu, D. Chen and Y. Feng, J. Hazard. Mater. **470**, 134259 (2024). doi:10.1016/j.jhazmat.2024.134259
[58] B. Weng, M. Zhang, Y. Lin, J. Yang, J. Lv, N. Han, J. Xie, H. Jia, B.-L. Su, M. Roeffaers, J. Hofkens, Y. Zhu, S. Wang, W. Choi and Y.-M. Zheng, Nat. Rev. Clean Technol. **1** (3), 201 (2025). doi:10.1038/s44359-025-00037-1
[59] C. Su, J. Hazard. Mater **322**, 48–84 (2017). doi:10.1016/j.jhazmat.2016.06.060
[60] L. Zhang, P. Li, Z. Gong and X. Li, J. Hazard. Mater. **158** (2–3), 478 (2008). doi:10.1016/j.jhazmat.2008.01.119
[61] H. Gupta and B. Gupta, Chemosphere **138**, 924 (2015). doi:10.1016/j.chemosphere.2014.12.028
[62] M.J. Silva, S.A.R. Soares, I.D.F. Santos, I.M. Pepe, L.R. Teixeira, L.G. Pereira, L.B.A. Silva and J. J. Celino, Heliyon **6** (10), e05163 (2020). doi:10.1016/j.heliyon.2020.e05163
[63] R. Wei, Y. Ge, H. Meng, G. Huang, J. Wu, F. Wen, H. Liu and X. Shen, Chem. Eng. J. **503**, 158352 (2025). doi:10.1016/j.cej.2024.158352
[64] S.R.D. Gamelas, J.P.C. Tomé, A.C. Tomé and L.M.O. Lourenço, RSC Adv. **13** (48), 33957 (2023). doi:10.1039/D3RA06598G
[65] D. Kanakaraju, P.P. Natashya, Y.-C. Lim and I.A.W. Tan, Environ. Monit. Assess. **197** (9), 983 (2025). doi:10.1007/s10661-025-14431-6
[66] M.E.A. Elsayed, H.A. Ayoub, M.I.D. Helal, W. Sang, Z. Shen and I.A. Abdelhafeez, Environ. Sci. Nano. **12** (4), 2128 (2025). doi:10.1039/D4EN00943F
[67] C. Chen, Z. Yuan, S. Sun, J. Xie, K. Zhang, Y. Zhai, R. Zuo, E. Bi, Y. Tao and Q. Song, Catalysts **14** (5), 311 (2024). doi:10.3390/catal14050311
[68] E. Lizundia, F. Luzi and D. Puglia, Green Chem. **24** (14), 5429 (2022). doi:10.1039/D2GC01668K
[69] D.A. Patiño-Ruiz, S.I. Meramo-Hurtado, A.D. González-Delgado and A. Herrera, ACS Omega. **6** (19), 12410 (2021). doi:10.1021/acsomega.0c05246
[70] A.T. Reda and Y.T. Park, Chem. Eng. J. **516**, 163894 (2025). doi:10.1016/j.cej.2025.163894